

# Correlations between oceanic crustal thickness, melt volume, and spreading rate from global gravity observation

Duo Zhou<sup>1</sup>, Chun-Feng Li<sup>1,2\*</sup>, Sergio Zlotnik<sup>3</sup>, Jian Wang<sup>4</sup>

<sup>1</sup>Institute of Marine Geology and Resources, Zhejiang University, Zhoushan, China.

<sup>2</sup>Laboratory for Marine Mineral Resources, Qingdao National Laboratory for Marine Science and Technology, Qingdao, China.

<sup>3</sup>Laboratori de Calcul Numèric, Escola Tècnica Superior d'Enginyers de Camins, Universitat Politècnica de Catalunya, Barcelona, Spain.

<sup>4</sup>Key Laboratory of Crustal Dynamics, Institute of Crustal Dynamics, China Earthquake Administration, Beijing, China.

\*Corresponding author: C.-F. Li ([cfl@zju.edu.cn](mailto:cfl@zju.edu.cn))

Ocean College, Zhejiang University, Zhoushan 316021, China.

Tel: 0086-0580-2092890 Fax: 0086-0580-2092891

## Abstract

Besides mantle depletion, oceanic crustal accretion at mid-ocean ridges is a function of spreading rate and mantle temperature, which are intertwined in affecting melt production and oceanic crustal thickness. Sparse and irregular seismic and geochemical observations on a global scale show no clear correlation between crustal thickness and spreading rate along slow to fast-spreading centers. Here, we compile a global oceanic crustal thickness model from gravity data to revisit this possible correlation at a higher resolution and a global scale. Gravity-observed melt volume shows a clear positive correlation with spreading rate, implying that spreading rate is

the dominant factor in melt production. However, we found a clear negative correlation between oceanic crustal thickness and spreading rate from slow to fast-spreading centers. This trend is further consolidated by increasing Curie point depth, a geothermal proxy, and ridge depth with increasing spreading rate. Thus, the decreasing mantle temperature probably also contributes to crustal thinning from slow to fast-spreading centers. Low inferred melt volumes beneath fast-spreading centers are consistent with a 20°C drop in mantle temperature, which may be caused by highly efficient hydrothermal cooling.

**Keywords:** Oceanic crustal thickness; Gravity inversion; Melt volume; Spreading rate; Mantle temperature; Hydrothermal circulation.

## 1. Introduction

Approximately 60% of the Earth's crust is formed by mantle decompression melting at mid-ocean ridges (Müller et al. 2008). The processes of oceanic crustal accretion vary with spreading rate (Christeson et al. 2019). At slow-spreading centers, magma supply is episodic (Bach and Fruh-Green 2010), with deep and rarely detectable magma chambers (Purdy et al. 1992; Searle 2013) and highly variable crustal thickness and seafloor morphology (Chen 1992; Lin and Morgan 1992). In contrast, at fast-spreading ridges, magma supply is stable (Christeson et al. 2019), with much shallower and more observable magma chambers, and relatively uniform crustal thickness and seafloor morphology (Lin and Morgan 1992). A variety of

parameters, such as mantle melting extent (Niu and Hékinian 1997) mantle upwelling rate (Forsyth 1992), and simulated melt volume (Bown and White 1994), correlate well with spreading rate. However, oceanic crustal thickness does not show a clear dependence on spreading rate, except for a decrease from slow to ultraslow-spreading centers (half spreading rate  $S_r < 10$  mm/yr) (Bown and White 1994; Chen 1992; Christeson et al. 2019; Dick et al. 2003; Jokat et al. 2003; Reid and Jackson 1981; White et al. 1992).

Crustal thickness observations by seismic experiments and geochemical measurements are sparse and scattered (Bown and White 1994; Chen 1992; Christeson et al. 2019; Reid and Jackson 1981; White et al. 1992), and more than half concentrate on ultraslow-spreading centers ( $S_r < 10$  mm/yr). Multiple seismic observations in old crust are probably modulated by lithospheric cooling effect (Christeson et al. 2019; Van Avendonk et al. 2016) or late tectonic events. Global seismic crustal models (e.g., Crust 1.0) (Laske et al. 2013) lack sufficient resolution to clearly resolve crustal thickness variations.

In contrast, satellite gravity observations provide a 2 arc min resolution on a global scale (Bonvalot et al. 2012). After excluding major density anomalies within oceanic lithosphere, residual gravity field could reflect the undulation of Moho interface (Li and Wang 2016). Therefore, crustal thicknesses derived from gravity data have a denser and more uniform global coverage compared with those from conventional methods (Searle 2013). The gravity approach has been widely applied to estimating Moho depths and variations of crustal thickness in various oceans (Alvey

et al. 2008; Lebedeva - Ivanova et al. 2019; Li and Wang 2016; Suo et al. 2016; Wang et al. 2011). For example, in the Atlantic Ocean, crustal thicknesses derived from gravity data are used to classify crust and track hotspots trails (Wang et al. 2011).

In this study, we compile a 10 km resolution global oceanic crustal thickness model based on 2 arc min satellite gravity data (Bonvalot et al. 2012). Then, crustal thicknesses are compared to spreading rate on crust younger than 5 Ma and more than 500 km from hotspots. Because temperature also affects mantle melting and oceanic crustal accretion (Langmuir and Forsyth 2007), we further investigate Curie point depth and water depth of mid-ocean ridge, both of which are geothermal proxies, and study their variations with spreading rate. We calculate gravity-derived melt volumes per unit time at different spreading centers and compare them with simulated volumes.

## **2. Residual complete Bouguer gravity anomalies**

### **2.1. Data**

The 2 arc min global free-air gravity model (WGM2012) (Bonvalot et al. 2012), which combines satellite-derived EGM2008 model (Pavlis et al. 2008) with updated Arctic gravity data (Andersen 2010), is used to estimate global Moho depth in this study. To avoid the potential circular logic between gravimetric correction and oceanic crustal thickness calculation, two bathymetric datasets were applied in our study. The one arc min global relief model ETOPO1 (Amante and Eakins, 2009), which integrates various global and regional datasets estimated from satellite

altimetry, was utilized for gravimetric corrections. The other one arc min minute global bathymetry model GEBCO (Tozer et al., 2019), without any estimation from gravity data, was adopted for thickness calculation, thus weakening the dependence on gravity signals. The global Curie point depth model of 10 arc min resolution (Li et al. 2017) is built from the magnetic anomaly model EMAG2 (Maus et al. 2009). Both global oceanic age and spreading rate model are with a resolution of 6 arc min from Müller et al (2008). Overall, age errors do not exceed 2 Ma along active spreading ridges.

## 2.2. Gravity Corrections

Residual complete Bouguer gravity anomalies mainly reflect Moho undulations, because Moho discontinuity has the largest density contrast in the lithosphere. Firstly, global complete Bouguer gravity anomaly is obtained after Bouguer slab correction (Bullard A), Earth's curvature correction (Bullard B), and terrain correction (Bullard C) (Fullea et al. 2008). Slab correction is based on an infinite plate model by assuming a density of  $1.03 \times 10^3 \text{ kg/m}^3$  for seawater and  $2.9 \times 10^3 \text{ kg/m}^3$  for oceanic crust. Curvature correction considers the curvature of the Earth's surface by shifting the infinite slab into a spherical cap with a radius of 167 km. Based on the distance between topography anomaly and calculation point, three zones are defined in terrain correction. The total correction of Bullard B and C is around  $\pm 10 \text{ mGal}$  in oceanic domain.

Secondly, thermal gravity correction is performed to remove the gravitational effect of oceanic lithospheric cooling. Based on the half-space cooling model

(Turcotte and Schubert 2002), temperature field ( $T$ ) of a 3-D thermal model (10×10×10 km<sup>3</sup> in grid size) of the oceanic lithosphere is given by

$$\frac{T - T_0}{T_m - T_0} = \operatorname{erf}\left(\frac{h}{2\sqrt{\kappa t}}\right), \quad (1)$$

where  $t$  is the oceanic age (Müller et al. 2008) and  $h$  is the lithospheric depth (Yoshii 1975). The parameters used in thermal correction are listed in Table 1. The thermal structure is transferred into a 3-D density contrast grid employing a thermal expansion equation, namely,

$$\Delta\rho = \alpha\rho_m (T_m - T). \quad (2)$$

**Table.1** Parameters applied in gravity corrections

Parameter	Definition	Value
$\rho_w$	Water density, kg m <sup>-3</sup>	$1.03 \times 10^3$
$\rho_c$	Crust density, kg m <sup>-3</sup>	$2.9 \times 10^3$
$\rho_m$	Mantle density, kg m <sup>-3</sup>	$3.3 \times 10^3$
$\kappa$	Thermal diffusivity, m <sup>2</sup> s <sup>-1</sup>	$10^{-6}$
$\alpha$	Volumetric thermal coefficient expansion, °C <sup>-1</sup>	$3 \times 10^{-5}$
$T_0$	Temperature at the plate surface, °C	0
$T_m$	Temperature at the plate bottom, °C	1300

The 3-D lithospheric thermal gravity anomaly can then be calculated from equations (1) and (2). Sedimentary correction is not needed, because our study mainly focuses on the active ridges, where sedimentary thicknesses are generally very thin (< 200 m) (Divins 2004).

### 3. Estimation of global oceanic crustal thickness

To estimate Moho depths, we apply Parker-Oldenburg iterative inversion method (Gómez-Ortiz and Agarwal 2005; Oldenburg 1974; Parker 1972), which links Fourier transform of gravity anomaly to that of Moho surface undulation. Moho density contrast and initial average Moho depth are two key input parameters for inversion. Gabbro density in the lowermost oceanic crust could reach 2.9-2.95 g/cm<sup>3</sup> (Rabbell et al. 2013), whereas empirical mantle density is 3.3 g/cm<sup>3</sup>. We adopt a constant global density contrast of 0.39 g/cm<sup>3</sup> across Moho. The initial Moho depth is tested between 18 and 28 km in a 0.5 km step, referring to the mean seismic global Moho depth of 23 km (Laske et al. 2013). Finally, the initial average Moho depth is set at 19.5 km below sea level, when our gravity-derived Moho agrees well with seismic Moho (Laske et al. 2013). To constrain long wavelength signals and improve the convergence of this iteration process, gravity data are filtered with a lower and upper cut-off wavenumber of 0.002 km<sup>-1</sup> and 0.012 km<sup>-1</sup>, respectively (Li and Wang 2016). The number of iterations is set at 150, large enough to make the difference in root-mean-square error between last two Moho depths lower than a convergence criteria 0.2 km.

Global oceanic crustal thicknesses from gravity inversion mostly range from 0 to 20 km and are independent of crustal age (Fig. 1). Overall, this model correlates well with seismic model Crust 1.0 (Laske et al. 2013) (Fig. 2a). While most seismic crustal thicknesses are narrowly concentrated on a mean value of 7 km (Fig. 2b), our

gravity-derived thickness can be best fitted by a sum of two normal distributions (Fig. 2c), one with a mean of 7.3 km from normal oceanic crustal thicknesses, and another with a mean of 13.5 km from seamounts, plateaus, volcanic chains, and ridges. These average values are consistent with seismic and geochemical observations (Searle 2013; White et al. 1992).

A uniform density contrast at the crust-mantle boundary may be biased, as local tectonic structures around mid-ocean ridge may affect gravity estimation. Firstly, mantle exhumation and serpentinization along ultraslow and slow-spreading ridges can result in low complete Bouguer gravity anomaly and apparently thin crust being inferred from gravity inversions. Nevertheless, its areal proportion is estimated to be only about 10% within 5 Ma isochrons along slow-spreading ridges (Tucholke et al. 2008). Secondly, beneath fast-spreading ridges, shallow (1.5-2 km) axial melting lens may also decrease complete Bouguer gravity anomaly, leading to large estimates of crustal thicknesses. However, the widths of axial melting lens are only around 4-7 km (Arnulf et al. 2014; Dunn et al. 2000), rather lower than the width of between two 5 Ma isochrons (500-1200 km). Furthermore, we exclude most abnormally thick or thin crust resulted from local tectonic structures by using a confidence interval (2.5 standard deviation within a spreading rate bin of 2 mm/yr). In summary, our gravity-derived result may not be as accurate as from local seismic measurements, but preserves the main features of seismic model, while providing a denser and more uniform coverage. Our model can be used to analyze thickness variation systematically on a global scale.



## 4. Crustal thickness, melt volume versus spreading rate

### 4.1. Crustal thickness versus spreading rate

According to previous studies (Searle 2013) and the distribution of gravity-derived crustal thickness at different half spreading rates  $S_r$  (Fig. 7), global mid-ocean ridges are divided into four categories, namely ultraslow ( $S_r < 10$  mm/yr), slow-medium ( $10 < S_r < 50$  mm/yr), fast ( $50 < S_r < 95$  mm/yr), and superfast ( $S_r > 95$  mm/yr) spreading ridges. The ultraslow and superfast-spreading ridges are further discussed in Appendix A. A broad variation of crustal thickness at slow-spreading centers can be observed, but we found a steady crustal thickness decrease, from 8.5 to 6.2 km on average, from slow to fast-spreading centers (Fig. 3;  $10 < S_r < 95$  mm/yr), which can be fitted with a linear regression. This observed trend seems to be opposite to previous models that showed increasing melting with increasing spreading rate (Fig. 3 inset b (Bown and White 1994)). However, in these numerical models, mantle potential temperature is assumed to be a constant 1300 °C. Additionally, the variation of melting area becomes relatively insensitive to increasing spreading rate when  $S_r > 10$  mm/yr (Fig. 3 inset b (Bown and White 1994)). The decreasing crustal thickness and insensitivity of melting area to spreading rate suggest that mantle potential temperature plays a major role in oceanic accretion at fast-spreading centers, as mantle temperature variation changes total melt volume and crustal thickness (Bown and White 1994; Langmuir and Forsyth 2007).

Curie point depth and ridge depth can be used to indicate mantle temperature (Dalton et al. 2014; Li et al. 2017; Wiens et al. 2006). Magnetic anomalies approximately follow the 550 °C isotherm (Li et al. 2013; Mayhew 1982; Tselentis 1991). Ridge depth variation, and its dependence on isostatic compensation, constrains the temperature of the asthenospheric mantle (Dalton et al. 2014; Turcotte and Schubert 2002). Within 5 Ma isochrons from slow to fast-spreading centers, Curie point depth deepens from 12.5 to 17.5 km on average (Fig. 4a). The same pattern holds within 1 Ma isochrons (Li et al. 2017). Meanwhile, average ridge depth increases progressively from 2.6 to 3.4 km (Fig. 4b). These trends demonstrate that mantle temperature decreases gradually from slow to fast-spreading ridges, probably causing decreasing oceanic crustal thickness. The stronger hydrothermal cooling effect with increasing spreading rate (Baker 2009; Baker et al. 1996; Li et al. 2017) might reduce mantle potential temperature and thin crust at fast-spreading centers (Morgan and Chen, 1994; Chen 2000; MacLennan et al. 2005).

#### 4.2. Melt volume versus spreading rate

Crustal thickness is a critical proxy of melt volume at ocean ridges, but melt volume per unit time is the product of oceanic crustal thickness and spreading width (Appendix B). Spreading width within two isochrons increases from slow to fast-spreading centers (10-95 km). Overall, the estimated melt volume increases linearly with increasing spreading rate (Fig. 5). Thus, decompression by seafloor spreading

primarily controls total melt production and dominates crustal accretion (Klein and Langmuir 1987; Langmuir et al. 1992).

Unexpectedly, our observed average melt volume drops noticeably when half spreading rate is larger than 50 mm/yr (Fig. 5). This slowdown of melt production rate indicates that other factors must constrain mantle melting at fast-spreading centers. To test this hypothesis, we first investigate the factor of temperature, since a reducing temperature pattern from slow to fast-spreading centers has already been revealed by Curie point and ridge depths (Fig. 4). Moreover, the linear decrease of MgO content with increasing spreading rate from global mid-ocean ridge basalts (Fig. 5 inset) (Rubin and Sinton 2007) suggests that eruptive temperatures at fast-spreading centers are roughly 20 °C lower than at slow-spreading centers (Coogan 2014).

To understand the temperature effect on melt volume, we estimate theoretical melt volumes using numerical modeling (Appendix B) and compare them with our results from gravity inversion. Overall, the simulated melt volume matches the observed volume well when the temperature at the base of the lithosphere ( $T_{lab}$ ) is fixed to 1330 °C (blue solid lines in Fig. 5 and Fig. 9), but again a discrepancy was observed at fast-spreading centers. Taking into account the temperature difference (20 °C) suggested by MgO analysis (Rubin and Sinton 2007), simulated melt volumes were recalculated at fast-spreading centers ( $50 < S_r < 95$  mm/yr) by decreasing  $T_{lab}$  to 1310 °C. Consequently, newly simulated volumes (red dash lines in Fig. 5 and S3) matches well with the gravity-derived results. We argue that the low temperature

anomaly (20 °C) restrains the melting beneath fast-spreading ridges, and overshadows the increase of melt volume from decompression.

## **5. Temperature modulation in oceanic crustal accretion**

### **5.1. Conductive versus hydrothermal cooling**

A 20 °C anomaly of mantle potential temperature is significant beneath fast-spreading centers, considering narrow variations (50-60 °C) along global mid-ocean ridges (Collier and Kelemen 2010; Kimura and Sano 2012; Niu and O'Hara 2008; Shen and Forsyth 1995), though wide variations (100-150 °C) are found deep beneath ridges (> 300 km) (Dalton et al. 2014). Compared with slow-spreading ridges, however, steady magma chamber with robust melt supply may provide more heat supply beneath fast-spreading centers, and the crust around known hotspots has already been excluded. Thus, this low 20 °C temperature anomaly at fast-spreading centers is probably caused by stronger heat loss than at slow-spreading centers. Young oceanic lithosphere suffers extensive heat loss through heat conduction and hydrothermal convection around the mid-ocean ridge (Stein and Stein 1994).

The timescale of conductive heat transfer is estimated to evaluate the efficiency of lithospheric conductive cooling. According to the relationship between thermal transfer conductivity, heat capacity, and thermal diffusivity ( $\kappa$ ) (Turcotte and Schubert 2002), the time of heat transfer ( $\Delta t$ ) is

$$\Delta t = \frac{L^2}{\kappa} . \quad (3)$$

Here  $L$  is the depth to the top of a heat source. Since the depth of axial melting lens decreases with increasing spreading rate (Coogan 2014), the minimum time of conductive heat transfer ( $\Delta t$ ) from axial melting lens to seafloor is expected at fast-spreading centers. If we set  $L = 1500$  m (Coogan 2014) and  $\kappa = 10^{-6}$  m<sup>2</sup>/s (Turcotte and Schubert 2002), the estimated  $\Delta t$  is more than 70,000 yr. This time of conductive heat loss is much longer than magmatic process in millennia to decades at ocean ridges (Brandl et al. 2016; Cannat et al. 2004; Rubin 2014). Considering the low efficiency of conductive cooling (Searle 2013), heat loss by lithospheric conduction can be neglected during the crustal accretion (Bown and White 1994).

Hydrothermal flow controls the shallow thermal structure beneath active mid-ocean ridges (Hasenclever et al. 2014). Approximately  $5 \times 10^{14}$  kg of seawater, heated from 2 to  $> 400$  °C, carries 30-50% of oceanic heat flux every year (Grose and Afonso 2015; Wolery and Sleep 1976) and decreases conductive heat flow dramatically within young oceanic lithosphere (Hasterok et al. 2011; Stein and Stein 1994). Furthermore, hydrothermal cooling becomes stronger with increasing spreading rate (Baker 2009; Baker et al. 1996; Li and Wang 2018). Especially at fast-spreading centers, seawater can penetrate deep gabbros (Cherkaoui et al. 2003; Dygert et al. 2017; Hasenclever et al. 2014; Nicolas et al. 2003; Theissen-Krah et al. 2016) and promote cooling rate by at least 2 order of magnitude in the lower crust (MacLennan et al. 2005; Sun and Lissenberg 2018). Additionally, hydrothermal convection can cool down axial melting lens from 1200 to 600 °C within decades (Fontaine et al. 2011; Zhang et al. 2014). Thus, highly efficient hydrothermal cooling

dominates heat loss of ocean ridges, limits magmatic process at ridge crests (e.g. Morgan and Chen, 1993; Chen, 2000; MacLennan et al. 2005), reduces mantle temperature and melt production beneath fast-spreading ridges.

## 5.2. Hydrothermal modulation on oceanic crustal thickness

Local geology (i.e. heat source and channels for seawater circulation within rocks) governs the power of hydrothermal circulation and cooling (Edmonds et al. 2003; Schmeling et al. 2017). Magma supply becomes more robust with increasing spreading rate (Coogan 2014; Perfit and Jr. Chadwick 1998). With shallower magma chambers and higher eruption frequency at fast-spreading centers, percolated seawater can be heated up more rapidly, and greatly enhance the incidence and intensity of hydrothermal activity (Baker 2009). Thus, seafloor massive sulfides (SMSs, percentage < 2%) can rarely be deposited and detected at fast-spreading centers, but they are abundant (> 98%) around slow and ultraslow-spreading ridges (Carbotte and Scheirer 2004).

Channels, including extensional faults, micro-cracks, and fissures, can efficiently increase the permeability of oceanic crust and promote hydrothermal circulation. Extensional faults generally develop in the brittle upper crust and end near the brittle-ductile boundary (800°C, Fig. 6a) (Manning et al. 1996; Wiens and Stein 1984). Therefore, extensional faults usually cannot get close to magma chamber with high temperatures (1000-1200°C). However, when dikes and upper gabbros are cooled by large quantities of seawater, plenty of micro-cracks can be generated by

thermal contraction of anisotropic gabbros in the ductile lower crust (Boudier et al. 2005; Nicolas et al. 2003). Meanwhile, the penetrated seawater would be heated rapidly ( $> 1000\text{ }^{\circ}\text{C}$ ) and increase the pressure greatly in the adjacent areas beneath fast-spreading ridges, when contracting micro-cracks extend around the shallow and wide magma chambers (Nicolas et al. 2003). Fronts of micro-cracks will induce plenty of hydro-fracturing fissures (Fig. 6a) (Manning et al. 2000; Nicolas et al. 2003). Extensional faults, micro-cracks, and fissures constitute a whole-crust fracture network beneath fast-spreading centers (Fig. 6a). The greatly increased permeability can promote the intensity of hydrothermal circulation to magma chamber effectively.

In contrast, micro-cracks at slow-spreading centers are generally far away from deep magma chamber and fail to generate hydro-fracturing fissures. Thus, most of hydrothermal circulations would be constrained in the upper crust (Fig. 6b), and hardly affect mantle melting beneath slow-spreading ridges. For example, cooling rate is estimated at  $10^{-3}$ - $10^{-4}\text{ }^{\circ}\text{C/yr}$  at the slow-spreading Mid-Atlantic ridge (Lissenberg et al. 2009), whereas at the fast-spreading East Pacific Rise it is estimated at  $10^{-2}\text{ }^{\circ}\text{C/yr}$  (Sun and Lissenberg 2018). Thus, with the whole-crust fracture network, hydrothermal circulations at fast-spreading centers may decrease the potential temperature and melt fraction of magma chamber effectively, causing regionally larger Curie point and ridge depths, smaller melt volume, and thinner oceanic crust.

## 6. Conclusion

Previous studies indicated that oceanic crustal thickness is independent of spreading rate from slow to fast-spreading centers. However, this viewpoint is limited by sparse and scattered measurements on a global scale. In this study, we provide a global oceanic crustal thickness model of a 10 km resolution based on gravity observations. Our new model preserves the main features of seismic model but offers a denser and more uniform coverage. After excluding the data influenced by hotspots ( $< 500$  km), oceanic crustal thicknesses between 0 and 5 Ma are compiled to re-correlate with spreading rate.

A steady decrease of oceanic crustal thickness is revealed from slow to fast-spreading centers. The linear trend correlates well with the variations of geothermal proxies, i.e. deepening Curie point depth and increasing ridge depth, both indicating that diminishing mantle temperature could be one of the major causes of the drop in oceanic crustal thickness and melt production. We estimate melt volume at different ridges based on our global crustal thickness model. Gravity-observed melt volume correlates well with spreading rate, since spreading rate is the primary controlling factor on total melt volume. Nevertheless, melt production rate slows down at fast-spreading centers (Fig. 5), which can be simulated with a lower mantle temperature by 20 °C, showing an effect of temperature on mantle melting.

We suggest that extensive hydrothermal circulations penetrate the whole-crust at fast-spreading centers. This efficient cooling process probably decreases mantle temperature, melt volume and oceanic crustal thickness. Mantle temperature has a



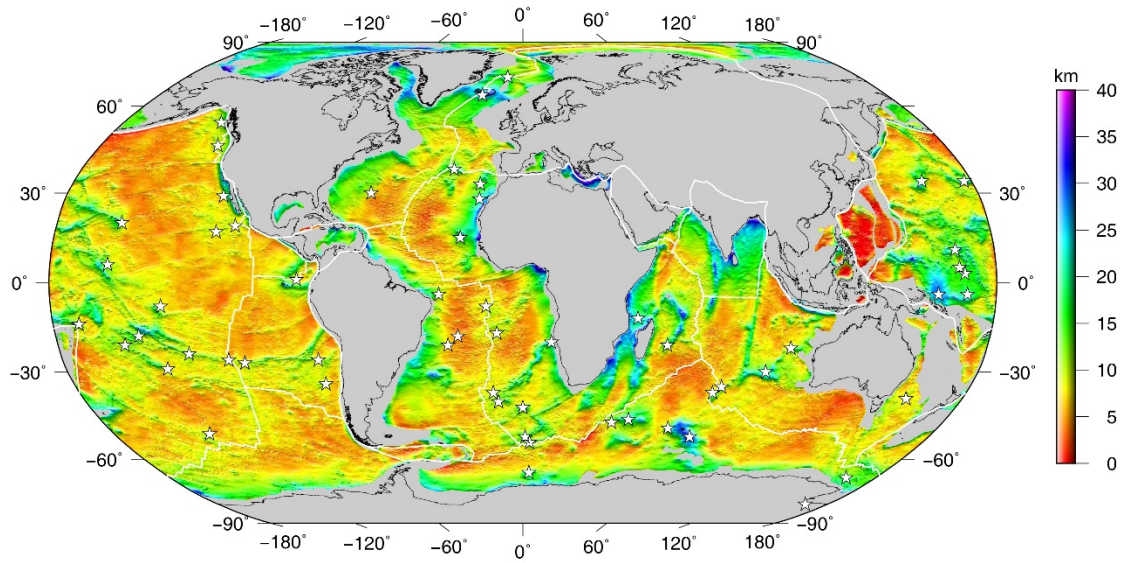
profound impact on the oceanic crustal accretion, particularly at fast-spreading centers.

### **Conflict of interest**

The authors declare that they have no conflict of interest.

### **Acknowledgments**

We thank Xiaobo He, Naifeng Fu, Alberto García González, and all members of Geodynamics Group at Zhejiang University for helpful discussions. This research is funded by National Natural Science Foundation of China (Grant No. 41776057, 41761134051, 41704086). Sergio Zlotnik thanks the funding from the Generalitat de Catalunya 2017-SGR-1278, the project DPI2017-85139-C2-2-R funded by the Spanish Ministry and the project H2020-RISE MATHROCKS (Grant agreement NO. 777778). Data processing and mapping are supported by MATLAB and GMT (Wessel & Smith, 1995).



349

350 **Fig. 1** The global oceanic crustal thickness model from gravity inversion. White lines  
 351 mark major plate boundaries (Demets et al. 1990). White stars show main oceanic  
 352 mantle hotspots (<http://www.mantleplumes.org/CompleteHotspot.html>)

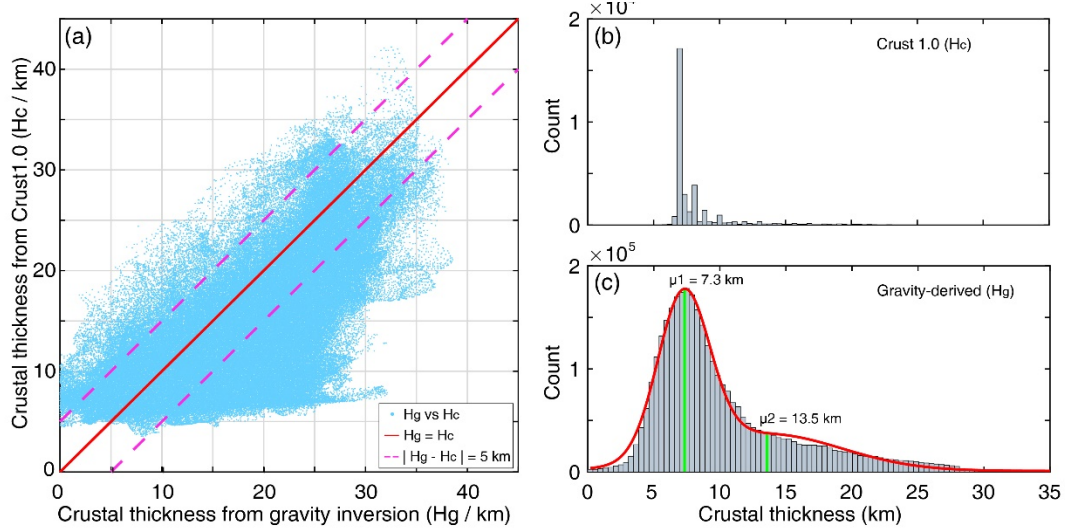


**Fig. 2** (a) The correlation of crustal thickness between our gravity-derived model and Crust1.0 model. (b) and (c) are distributions of crustal thickness from Crust1.0 model and our gravity inversion, respectively. Our gravity-derived thicknesses can be best fitted by a mixture of two normal distributions, with mean and standard deviations at 7.3 km and 2.8 km, and 13.5 km and 8.1 km, respectively. The percentage of the first normal distribution is 0.81 and the second is 0.19

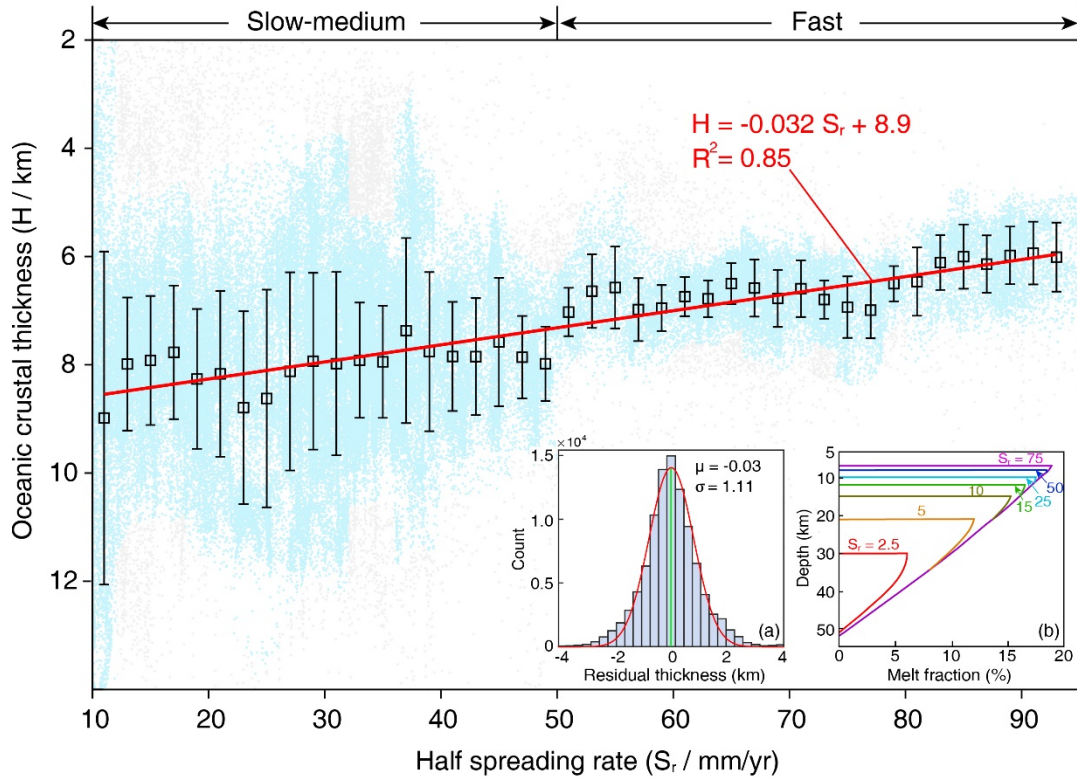
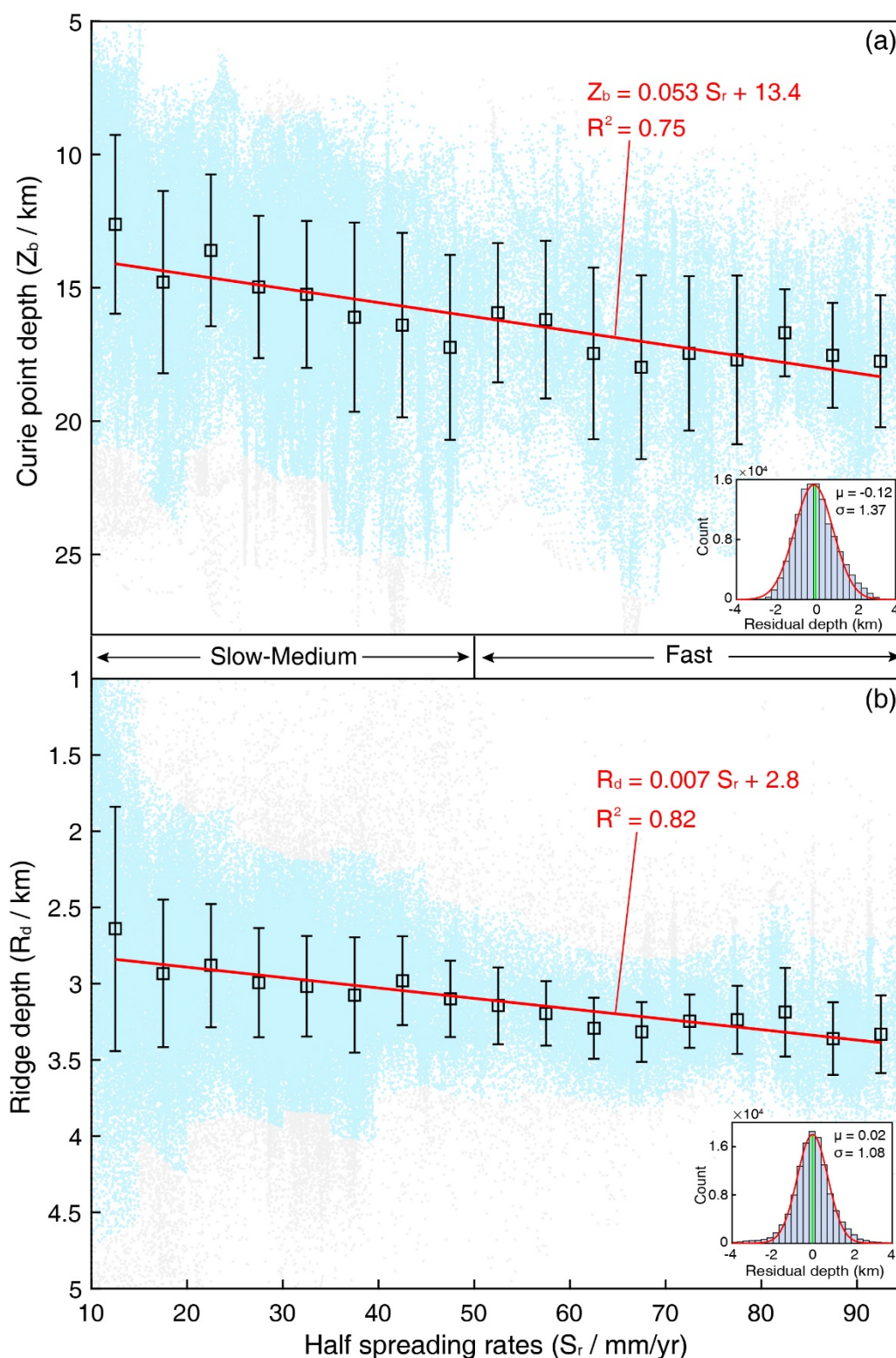


**Fig. 3** Crustal thickness ( $H$ ) variation with spreading rate ( $S_r$ ) within 5 Ma isochrons ( $10 < S_r < 95$  mm/yr). Data points within a radius of 500 km around hotspots are removed (Fig. 1). The means (open squares) and standard deviations (black error bars) are based on colored dots those are within 2.5 times standard deviation of the linear trend in each confidence interval (2 mm/yr). The red solid line is a linear regression of the mean values of  $H$ . The inset (a) shows an approximately standard normal distribution of the standardized residual  $H$  for light blue data points, indicating a robust linear regression from slow to fast-spreading centers. The inset (b) modified from Bown and White (1994) shows different mantle melt fraction below ridges predicted at different half spreading rates (mm/yr) with a constant mantle potential temperature of 1300°C. Melting volume can be estimated from triangular areas at different spreading rates



374

375 **Fig. 4** Curie point depth and ridge depth correlations with spreading rate ( $10 < S_r < 95$   
 376 mm/yr). (a) Curie depths ( $Z_b$ ) within 5 Ma isochrons of active spreading centers are  
 377 from the global reference model of Curie depth (Li et al. 2017). (b) Ridge depth ( $R_d$ )

378 variation with spreading rate ( $S_r$ ) within 5 Ma isochrons of active spreading centers  
379 from the SRTM30+ model (Becker et al. 2009). The means (open squares) and  
380 standard deviations (black error bars) are based on colored dots that are within 2.5  
381 times standard deviation of linear trend in each confidence interval. The red solid  
382 lines are linear regressions of mean values of  $Z_b$  and  $R_d$  for  $10 < S_r < 95$  mm/yr and  $S_r$   
383  $> 95$  mm/yr, respectively. Two insets show two approximate standard normal  
384 distributions of standardized residual  $Z_b$  and  $R_d$  for light blue data points, indicating  
385 robust linear regressions from slow to fast-spreading centers



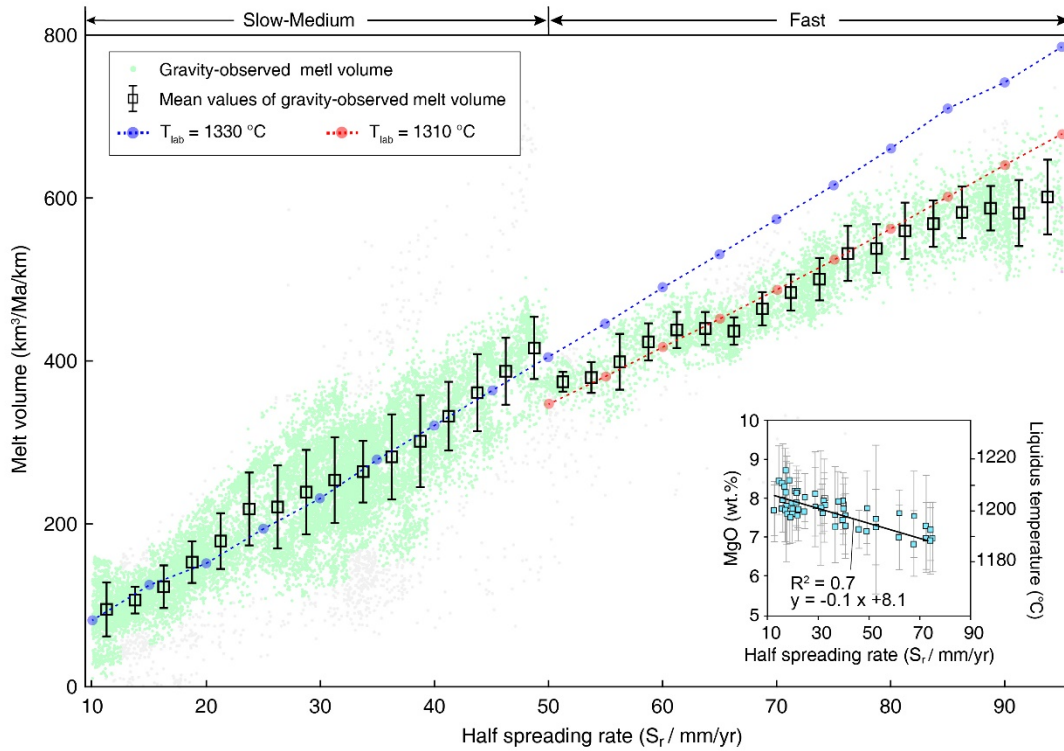


**Fig. 5** Melt volume variation with half spreading rate along mid-ocean ridges within 1 Ma isochrons for a 1 km length segment ( $10 < S_r < 95$  mm/yr). Gravity-observed melt volume is estimated from the product of crustal thickness and spreading rate (Appendix B.1). The means (open squares) of gravity-derived melt volumes and standard deviations (black error bars) are based on colored dots that are within 2.5 times standard deviation of the linear trend in each confidence interval. Blue and red dotted lines with corresponding circles are from numerical modeling at different spreading rates.  $T_{\text{lab}}$  represents the temperature at the base of the lithosphere. The inset shows that liquidus temperature varies with half spreading rate based on MgO content in the MORB (Rubin and Sinton 2007)

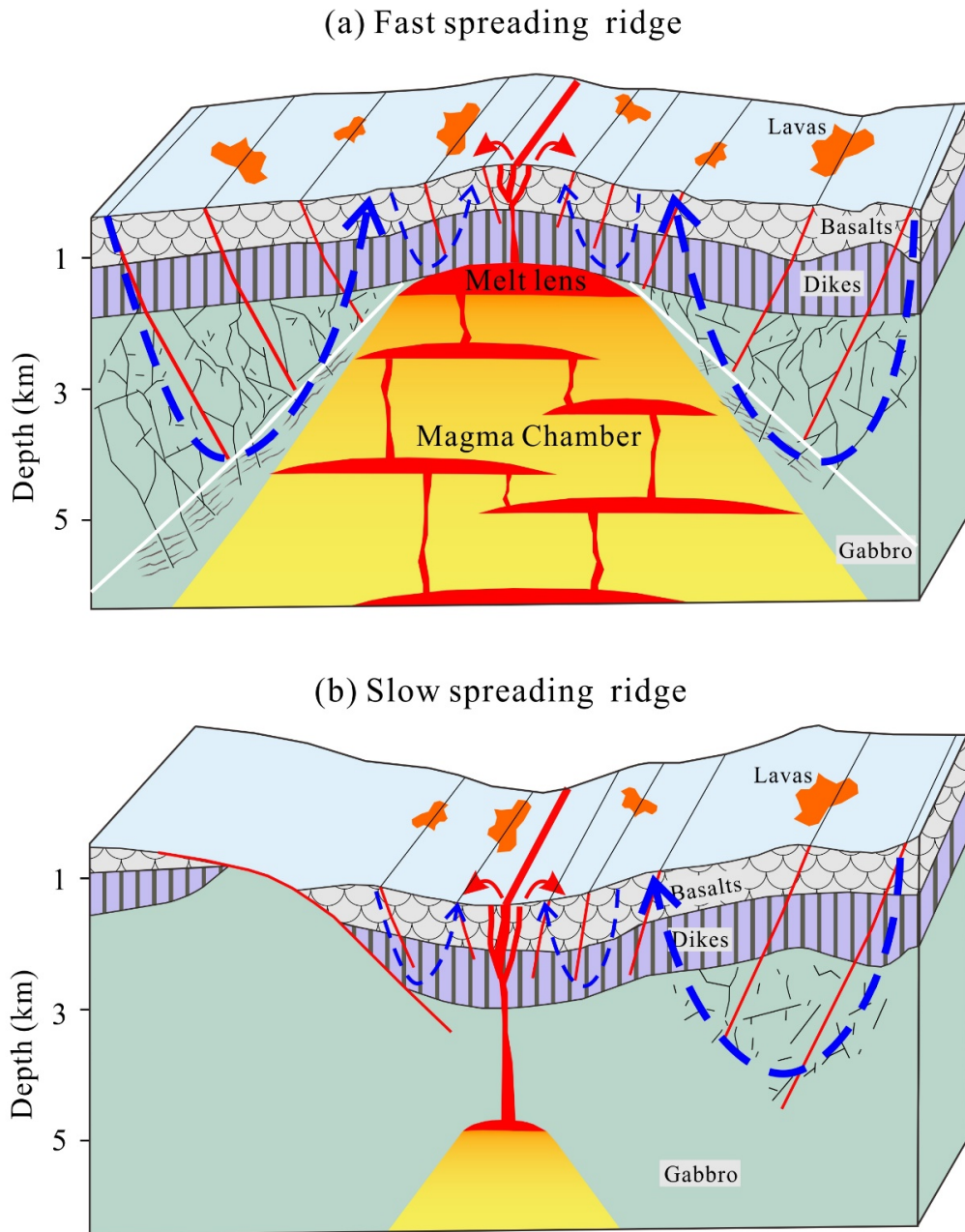


**Fig. 6** Schematic models of crustal accretion at fast (a) and slow (b) spreading centers, modified from Sinton and Detrick (1992) and Coogan (2014). The dashed blue lines with arrows display hydrothermal circulations beneath ridges. The white line in (a) represents the ductile brittle transition boundary inferred from B  cel et al. (2015). The thin black lines are micro-cracks within gabbros. The grey filled lines around the chamber wall in (a) represent hydro-fracturing fissures



## 405 Reference

- 406 Alvey A, Gaina C, Kuszniir NJ, Torsvik TH (2008) Integrated crustal thickness mapping and plate  
407 reconstructions for the high Arctic. *Earth Planet Sci Lett* 274:310-321  
408 doi:10.1016/j.epsl.2008.07.036
- 409 Amante C, Eakins BW (2009) ETOPO1 1 arc minute global relief model procedures, data sources and  
410 analysis. NOAA Technical Memorandum NESDIS NGDC-24, NOAA
- 411 Andersen OB The DTU10 Global Gravity field and mean sea surface – improvements in the Arctic. In:  
412 2nd IGFS meeting, Fairbanks, Alaska., 2010.
- 413 Arnulf AF, Singh SC, Pye JW (2014) Seismic evidence of a complex multi-lens melt reservoir beneath  
414 the 9° N Overlapping Spreading Center at the East Pacific Rise. *Geophys Res Lett* 41:6109-  
415 6115 doi:10.1002/2014gl060859
- 416 Bach W, Fruh-Green GL (2010) Alteration of the Oceanic Lithosphere and Implications for Seafloor  
417 Processes. *Elements* 6:173-178 doi:10.2113/gselements.6.3.173
- 418 Baker ET (2009) Relationships between hydrothermal activity and axial magma chamber distribution,  
419 depth, and melt content. *Geochem Geophys Geosyst* 10:n/a-n/a doi:10.1029/2009gc002424
- 420 Baker ET, John. CY, Morgan JP (1996) The relationship between near-axis hydrothermal cooling and  
421 the spreading rate of mid-ocean ridges. *Earth Planet Sci Lett* 142:137-145
- 422 Bécel A, Shillington DJ, Nedimović MR, Webb SC, Kuehn H (2015) Origin of dipping structures in  
423 fast-spreading oceanic lower crust offshore Alaska imaged by multichannel seismic data.  
424 *Earth Planet Sci Lett* 424:26-37 doi:10.1016/j.epsl.2015.05.016
- 425 Becker JJ et al. (2009) Global Bathymetry and Elevation Data at 30 Arc Seconds Resolution:  
426 SRTM30\_PLUS. *Mar Geod* 32:355-371 doi:10.1080/01490410903297766
- 427 Bonvalot S et al. (2012) World Gravity Map. Bureau Gravimétrique International (BGI), Paris
- 428 Boudier F, Nicolas A, Mainprice D (2005) Does Anisotropy of Thermal Contraction Control  
429 Hydrothermal Circulation at the Moho Level below Fast Spreading Oceanic Ridges? *Int Geol*  
430 *Rev* 47:101-112 doi:10.2747/0020-6814.47.1.101
- 431 Bown JW, White RS (1994) Variation with spreading rate of oceanic crustal thickness and  
432 geochemistry. *Earth Planet Sci Lett* 121:435-449
- 433 Brandl PA, Regelous M, Beier C, O'Neill HSC, Nebel O, Haase KM (2016) The timescales of magma  
434 evolution at mid-ocean ridges. *Lithos* 240-243:49-68 doi:10.1016/j.lithos.2015.10.020
- 435 Cannat M, Cann J, MacLennan J (2004) Some Hard Rock Constraints on the Supply of Heat to Mid -  
436 Ocean Ridges. In: German CR, Lin J, Parson LM (eds) *Mid-Ocean Ridges: Hydrothermal*  
437 *Interactions Between the Lithosphere and Oceans*. American Geophysical Union, pp 111-149.  
438 doi:<https://doi.org/10.1029/148GM05>
- 439 Carbotte SM, Scheirer DM (2004) Variability of ocean crustal structure created along the global mid-  
440 ocean ridge. In: Davis EE, Elderfi eld H (eds) *Hydrogeology of the oceanic lithosphere*:  
441 Cambridge. Cambridge University Press, UK, pp 59–107
- 442 Chen YJ (1992) Ocean crustal thickness versus spreading rate. *Geophys Res Lett* 19:753-756  
443 doi:<https://doi.org/10.1029/92GL00161>
- 444 Cherkaoui ASM, Wilcock WSD, Dunn RA, Toomey DR (2003) A numerical model of hydrothermal  
445 cooling and crustal accretion at a fast spreading mid-ocean ridge. *Geochem Geophys Geosyst*  
446 4:8616 doi:10.1029/2001GC000215
- 447 Christeson GL, Goff JA, Reece RS (2019) Synthesis of Oceanic Crustal Structure From Two -  
448 Dimensional Seismic Profiles. *Rev Geophys* 57:504-529 doi:10.1029/2019rg000641
- 449 Collier ML, Kelemen PB (2010) The Case for Reactive Crystallization at Mid-Ocean Ridges. *J Petrol*  
450 51:1913-1940 doi:10.1093/petrology/egq043
- 451 Coogan LA (2014) The Lower Oceanic Crust. In: *Treatise on Geochemistry*. pp 497-541.  
452 doi:10.1016/b978-0-08-095975-7.00316-8
- 453 Dalton CA, Langmuir CH, Gale A (2014) Geophysical and Geochemical Evidence for Deep  
454 Temperature Variations Beneath Mid-Ocean Ridges. *Science* 344:80-83  
455 doi:<https://doi.org/10.1126/science.1249466>
- 456 Demets C, Gordon RG, Argus DF, Stein S (1990) Current plate motions. *Geophys J Int* 101:425-478  
457 doi:<https://doi.org/10.1111/j.1365-246X.1990.tb06579.x>
- 458 Dick HJB, Lin J, Schouten H (2003) An ultraslow-spreading class of ocean ridge. *Nature* 426 405–412  
459 doi:10.1038/nature02128
- 460 Divins DL (2004) Total Sediment Thickness of the World's Oceans and Marginal Seas. NOAA  
461 National Geophysical Data Center: Boulder.

- Dunn RA, Toomey DR, Solomon SC (2000) Three-dimensional seismic structure and physical properties of the crust and shallow mantle beneath the East Pacific Rise at 9°30'N. *J Geophys Res Solid Earth* 105:23537-23555 doi:10.1029/2000jb900210
- Dygart N, Kelemen PB, Liang Y (2017) Spatial variations in cooling rate in the mantle section of the Samail ophiolite in Oman: Implications for formation of lithosphere at mid-ocean ridges. *Earth Planet Sci Lett* 465:134-144 doi:10.1016/j.epsl.2017.02.038
- Edmonds HN et al. (2003) Discovery of abundant hydrothermal venting on the ultraslow-spreading Gakkel ridge in the Arctic Ocean. *Nature* 421:252-256 doi:10.1038/nature01351
- Fontaine FJ, Olive J-A, Cannat M, Escartin J, Perol T (2011) Hydrothermally-induced melt lens cooling and segmentation along the axis of fast- and intermediate-spreading centers. *Geophys Res Lett* 38:n/a-n/a doi:10.1029/2011gl047798
- Forsyth DW (1992) Geophysical Constraints on Mantle Flow and Melt Generation Beneath Mid-Ocean Ridges. In: Morgan JP, Blackman DK, Sinton JM (eds) *Mantle Flow and Melt Generation at Mid-Ocean Ridges*. Washington DC, pp 1-66
- Fullea J, Fernández M, Zeyen H (2008) FA2BOUG—A FORTRAN 90 code to compute Bouguer gravity anomalies from gridded free-air anomalies: Application to the Atlantic-Mediterranean transition zone. *Comp Geosci* 34:1665-1681 doi:10.1016/j.cageo.2008.02.018
- Gómez-Ortiz D, Agarwal BNP (2005) 3DINVER.M: a MATLAB program to invert the gravity anomaly over a 3D horizontal density interface by Parker–Oldenburg's algorithm. *Comp Geosci* 31:513-520 doi:10.1016/j.cageo.2004.11.004
- Grose CJ, Afonso JC (2015) The hydrothermal power of oceanic lithosphere. *Solid Earth* 6:1131-1155 doi:10.5194/se-6-1131-2015
- Hasenclever J, Theissen-Krah S, Rupke LH, Morgan JP, Iyer K, Petersen S, Devey CW (2014) Hybrid shallow on-axis and deep off-axis hydrothermal circulation at fast-spreading ridges. *Nature* 508:508-512 doi:10.1038/nature13174
- Hasterok D, Chapman DS, Davis EE (2011) Oceanic heat flow: Implications for global heat loss. *Earth Planet Sci Lett* 311:386-395 doi:10.1016/j.epsl.2011.09.044
- Jokat W, Ritzmann O, Schmidt-Aursch MC, Drachev S, Gauger S, Snow J (2003) Geophysical evidence for reduced melt production on the Arctic ultraslow Gakkel mid-ocean ridge. *Nature* 423:962-965 doi:10.1038/nature01706
- Kimura JI, Sano S (2012) Reactive Melt Flow as the Origin of Residual Mantle Lithologies and Basalt Chemistries in Mid-Ocean Ridges: Implications from the Red Hills Peridotite, New Zealand. *J Petrol* 53:1637-1671 doi:10.1093/petrology/egs028
- Klein EM, Langmuir CH (1987) Global correlations of ocean ridge basalt chemistry with axial depth and crustal thickness. *J Geophys Res* 92 doi:10.1029/JB092iB08p08089
- Langmuir CH, Forsyth DW (2007) Mantle Melting Beneath Mid-Ocean Ridges. *Oceanography* 20:78-89
- Langmuir CH, Klein EM, Plank T (1992) Petrological Systematics of Mid-Ocean Ridge Basalts: Constraints on Melt Generation Beneath Ocean Ridges. In: Morgan JP, Blackman DK, Sinton JM (eds) *Mantle Flow and Melt Generation at Mid-Ocean Ridges*, vol 71. American Geophysical Union, pp 183– 280
- Laske G, Masters G, Ma Z, Pasyanos M (2013) Update on CRUST1.0 - A 1-degree global model of Earth's crust. Paper presented at the EGU, Vienna, Austria,
- Lebedeva - Ivanova N, Gaina C, Minakov A, Kashubin S (2019) ArcCRUST: Arctic Crustal Thickness From 3 - D Gravity Inversion. *Geochem Geophys Geosyst* doi:10.1029/2018gc008098
- Li C-F, Lu Y, Wang J (2017) A global reference model of Curie point depths based on EMAG2. *Sci Rep* 7:45129 doi:10.1038/srep45129
- Li C-F, Wang J (2016) Variations in Moho and Curie depths and heat flow in Eastern and Southeastern Asia. *Mar Geophys Res* 37:1-20 doi:10.1007/s11001-016-9265-4
- Li C-F, Wang J (2018) Thermal structures of the Pacific lithosphere from magnetic anomaly inversion. *Earth and Planetary Physics* 2:1-15 doi:10.26464/epp2018005
- Li C-F, Wang J, Lin J, Wang T (2013) Thermal evolution of the North Atlantic lithosphere: New constraints from magnetic anomaly inversion with a fractal magnetization model. *Geochem Geophys Geosyst* 14:5078-5105 doi:10.1002/2013gc004896
- Lin J, Morgan JP (1992) The spreading rate dependence of three - dimensional mid - ocean ridge gravity structure. *Geophys Res Lett* 19:13-16 doi:10.1029/91GL03041
- Lissenberg CJ, Rioux M, Shimizu N, Bowring SA, Mével C (2009) Zircon Dating of Oceanic Crustal Accretion. *Science* 323:1045-1048 doi:<https://doi.org/10.1126/science.1165675>
- Lister CRB (1972) On the Thermal Balance of a Mid-Ocean Ridge. *Geophys J Int* 26:515-535 doi:<https://doi.org/10.1111/j.1365-246X.1972.tb05766.x>

- MacLennan J, Hulme T, Singh SC (2005) Cooling of the lower oceanic crust. *Geology* 33 doi:10.1130/g21207.1
- Manning CE, MacLeod CJ, Weston PE (2000) Lower-crustal cracking front at fast-spreading ridges: Evidence from the East Pacific Rise and the Oman ophiolite. *Geol Soc Am Bull* 349:261–272
- Manning CE, Weston PE, Mahon KI (1996) Rapid high-temperature metamorphism of East Pacific Rise gabbros from Hess Deep. *Earth Planet Sci Lett* 1:123-132 doi:[https://doi.org/10.1016/0012-821X\(96\)00153-7](https://doi.org/10.1016/0012-821X(96)00153-7)
- Maus S et al. (2009) EMAG2: A 2-arc min resolution Earth Magnetic Anomaly Grid compiled from satellite, airborne, and marine magnetic measurements. *Geochem Geophys Geosyst* 10:n/a-n/a doi:10.1029/2009gc002471
- Mayhew MA (1982) Application of satellite magnetic anomaly data to Curie isotherm mapping. *J Geophys Res* 87:4846-4854 doi:<https://doi.org/10.1029/JB087iB06p04846>
- Müller RD, Sdrolias M, Gaina C, Roest WR (2008) Age, spreading rates, and spreading asymmetry of the world's ocean crust. *Geochem Geophys Geosyst* 9:n/a-n/a doi:10.1029/2007gc001743
- Nicolas A, Mainprice D, Boudier Fo (2003) High-temperature seawater circulation throughout crust of oceanic ridges: A model derived from the Oman ophiolites. *J Geophys Res* 108 doi:10.1029/2002jb002094
- Niu Y, Hékinian R (1997) Spreading-rate dependence of the extent of mantle melting beneath ocean ridges. *Nature* 385:326-329 doi:<https://doi.org/10.1038/385326a0>
- Niu Y, O'Hara MJ (2008) Global Correlations of Ocean Ridge Basalt Chemistry with Axial Depth: a New Perspective. *J Petrol* 49:633-664 doi:10.1093/petrology/egm051
- Oldenburg DW (1974) Inversion and interpretation of the gravity anomalies. *Geophysics* 39:526-536 doi:<https://doi.org/10.1190/1.1440444>
- Parker RL (1972) Rapid calculation of potential anomalies. *Geophys J Int* 31:447-455 doi:<https://doi.org/10.1111/j.1365-246X.1973.tb06513.x>
- Pavlis NK, Factor JK, Holmes. SA (2008) An Earth gravitational model to degree 2160: EGM 2008. Paper presented at the General Assembly of the European Geosciences Union, Vienna, Austria.,
- Perfit MR, Jr. Chadwick WW (1998) Magmatism at Mid-Ocean Ridges' Constraints from Volcanological and Geochemical Investigations. In: Lagabriele WRBP (ed) *Faulting and Magmatism at Mid - Ocean Ridges*, vol 106. American Geophysical Union, pp 59-115
- Purdy G, Kong L, Christeson G, Solomon S (1992) Relationship between spreading rate and the seismic structure of mid-ocean ridges. *Nature* 355:815-817 doi:<https://doi.org/10.1038/355815a0>
- Rabbet W, Kaban M, Tesauro M (2013) Contrasts of seismic velocity, density and strength across the Moho. *Tectonophysics* 609:437-455 doi:10.1016/j.tecto.2013.06.020
- Reid I, Jackson HR (1981) Oceanic spreading rate and crustal thickness. *Mar Geophys Res* 5:165-172 doi:<https://doi.org/10.1007/BF00163477>
- Rubin KH (2014) Mid-Ocean Ridge Magmatism and Volcanism. In: *Encyclopedia of Marine Geosciences*. pp 1-21. doi:10.1007/978-94-007-6644-0\_28-3
- Rubin KH, Sinton JM (2007) Inferences on mid-ocean ridge thermal and magmatic structure from MORB compositions. *Earth Planet Sci Lett* 260:257-276 doi:10.1016/j.epsl.2007.05.035
- Schmeling H, Marquart G, Nawa V (2017) The role of hydrothermal cooling of the oceanic lithosphere for ocean floor bathymetry and heat flow. *J Geophys Res Solid Earth* 122:3934-3952 doi:10.1002/2016jb013881
- Searle R (2013) *Mid-Ocean Ridges*. Cambridge University Press, Cambridge
- Shen Y, Forsyth D (1995) Geochemical constraints on initial and final depths of melting beneath mid-ocean ridges. *J Geophys Res* 100:2211-2237 doi:<https://doi.org/10.1029/94JB02768>
- Sinton JM, Detrick RS (1992) Mid-ocean ridge magma chambers. *J Geophys Res* 97:197-216 doi:<https://doi.org/10.1029/91JB02508>
- Stein CA, Stein S (1994) Constraints on hydrothermal heat flux through the oceanic lithosphere from global heat flow. *J Geophys Res Solid Earth* 99:3081-3095 doi:<https://doi.org/10.1029/93JB02222>
- Sun C, Lissenberg CJ (2018) Formation of fast-spreading lower oceanic crust as revealed by a new Mg-REE coupled geospeedometer. *Earth Planet Sci Lett* 487:165-178 doi:10.1016/j.epsl.2018.01.032
- Suo Y, Li S, Li X, Guo L, Wang Y (2016) Crustal thickness anomalies in the Indian Ocean inferred from gravity analysis. *Geol J* 51:634-643 doi:10.1002/gj.2786
- Theissen-Krah S, Rüpke LH, Hasenclever J (2016) Modes of crustal accretion and their implications for hydrothermal circulation. *Geophys Res Lett* 43:1124-1131 doi:10.1002/2015gl067335

- Tozer B, Sandwell DT, Smith WHF, Olson C, Beale JR, Wessel P (2019) Global bathymetry and topography at 15 arc seconds: 2 SRTM15+. *Earth Space Sci* 6:1847-1864 doi:10.1029/2019EA000658
- Tselentis (1991) An attempt to define Curie point depths in Greece from aeromagnetic and heat flow data. *Pure Appl Geophys* 136:87-101
- Tucholke BE, Behn MD, Buck WR, Lin J (2008) Role of melt supply in oceanic detachment faulting and formation of megamullions. *Geology* 36 doi:10.1130/g24639a.1
- Turcotte DL, Schubert G (2002) *Geodynamics*. Second Edition edn. Cambridge University Press,
- Van Avendonk HJA, Davis JK, Harding JL, Lawver LA (2016) Decrease in oceanic crustal thickness since the breakup of Pangaea. *Nat Geosci* 10:58-61 doi:10.1038/ngeo2849
- Wang T, Lin J, Tucholke B, Chen YJ (2011) Crustal thickness anomalies in the North Atlantic Ocean basin from gravity analysis. *Geochem Geophys Geosyst* 12:n/a-n/a doi:10.1029/2010gc003402
- White RS, McKenzie D, O'Nions RK (1992) Oceanic crustal thickness from seismic measurements and rare earth element inversions. *J Geophys Res* 97 doi:10.1029/92jb01749
- Wiens DA, Kelley KA, Plank T (2006) Mantle temperature variations beneath back-arc spreading centers inferred from seismology, petrology, and bathymetry. *Earth Planet Sci Lett* 248:30-42 doi:10.1016/j.epsl.2006.04.011
- Wiens DA, Stein S (1984) Intraplate seismicity and stresses in young oceanic lithosphere. *J Geophys Res* 89:11,442-411,464, doi:<https://doi.org/10.1029/JB089iB13p11442>
- Wolery TJ, Sleep NH (1976) Hydrothermal Circulation and Geochemical Flux at Mid-Ocean Ridges. *THE JOURNAL OF GEOLOGY* 84:249-275
- Yoshii T (1975) Regionality of group velocities of Rayleigh-waves in pacific and thickening of plate. *Earth Planet Sci Lett* 25:305-312 doi:[https://doi.org/10.1016/0012-821X\(75\)90246-0](https://doi.org/10.1016/0012-821X(75)90246-0)
- Zhang C, Koepke J, Kirchner C, Gotze N, Behrens H (2014) Rapid hydrothermal cooling above the axial melt lens at fast-spreading mid-ocean ridge. *Sci Rep* 4:6342 doi:10.1038/srep06342

## **APPENDIX A: On ultraslow and superfast-spreading centers**

### **A.1 Ultraslow-spreading Centers**

Our estimated oceanic crustal thicknesses decrease rapidly when spreading rate gets smaller at ultraslow ridges ( $S_r < 10$  mm/yr) (Fig. 7), consistent with seismic (Chen 1992; Reid and Jackson 1981) and geochemical results (White et al. 1992). The top of the melting region can reach a depth of 30 km as spreading rate decreases to 2.5 mm/yr (Fig. 7 inset b) (Bown and White 1994). These trends correspond to increasing Curie point depth (from 12 to 14 km, Fig. 8a) and ridge depth (from 3 to 3.7 km, Fig. 8b). Besides, most oceanic crust thinner than 5 km were found at ultraslow-spreading ridges (Fig. 7) due to low melt production ( $< 100$  km<sup>3</sup>/Ma/km, Fig. 9) caused by significant conductive heat loss (White et al. 2001). Furthermore, an exclusive oblique spreading pattern at ultraslow-spreading centers, e.g., the Arctic ridge, could weaken decompression effect and reduce melt production (Dick et al. 2003).

### **A.2 Superfast-spreading Centers**

From fast to superfast-spreading ridges ( $S_r > 95$  mm/yr), mean crustal thickness increases rapidly from 6 to 8 km (Fig. 7). This trend is consistent with decreasing Curie point and ridge depths (Fig. 8) and increasing melt volume (Fig. 9). Abundant magma supplies at superfast-spreading ridges result in a much higher extrusive to intrusive ratio than that at fast-spreading ridges. For example, at fast-spreading East Pacific Rise ( $S_r = 65$  mm/yr), the Deep Sea Drilling Project at Hess Deep reveals that extrusive lavas are usually thinner than sheeted dikes (Dick et al. 1992). However, at

629 the superfast-spreading East Pacific Rise ( $S_r = 110$  mm/yr), Umino et al. (2008) found  
630 a very thick sequence of extrusive rocks (881 m) overlying a thin sheeted dike of  
631 intrusive rocks (346 m) in Ocean Drilling Program Hole 1256D. Here strong  
632 decompression melting, which produces large melt volumes (Fig. 9) and high ridge  
633 temperatures (Li et al. 2017), dominates the formation of oceanic crust.  
634



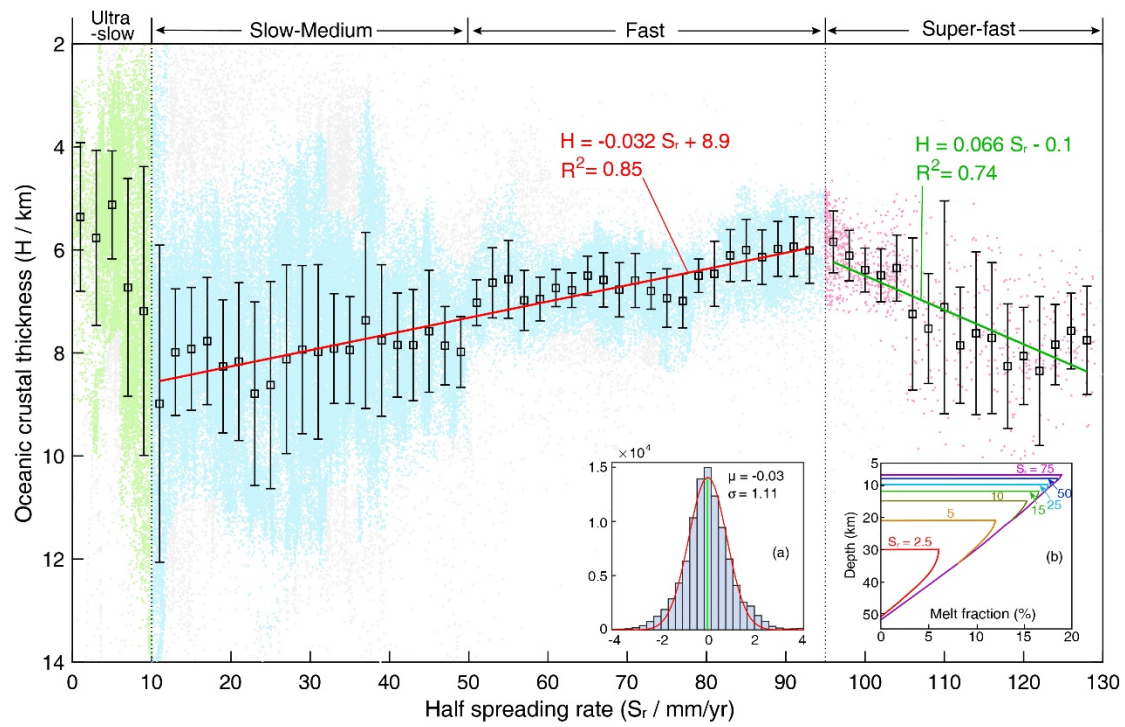


**Fig. 7** Crustal thickness ( $H$ ) variation with spreading rate ( $S_r$ ) within 5 Ma isochrons. Data points within a radius of 500 km around hotspots are removed (Fig. 1). The red and green solid lines are linear regressions of mean values of  $H$  for  $10 < S_r < 95$  mm/yr and  $S_r > 95$  mm/yr, respectively. Other label interpretations refer to Fig. 3

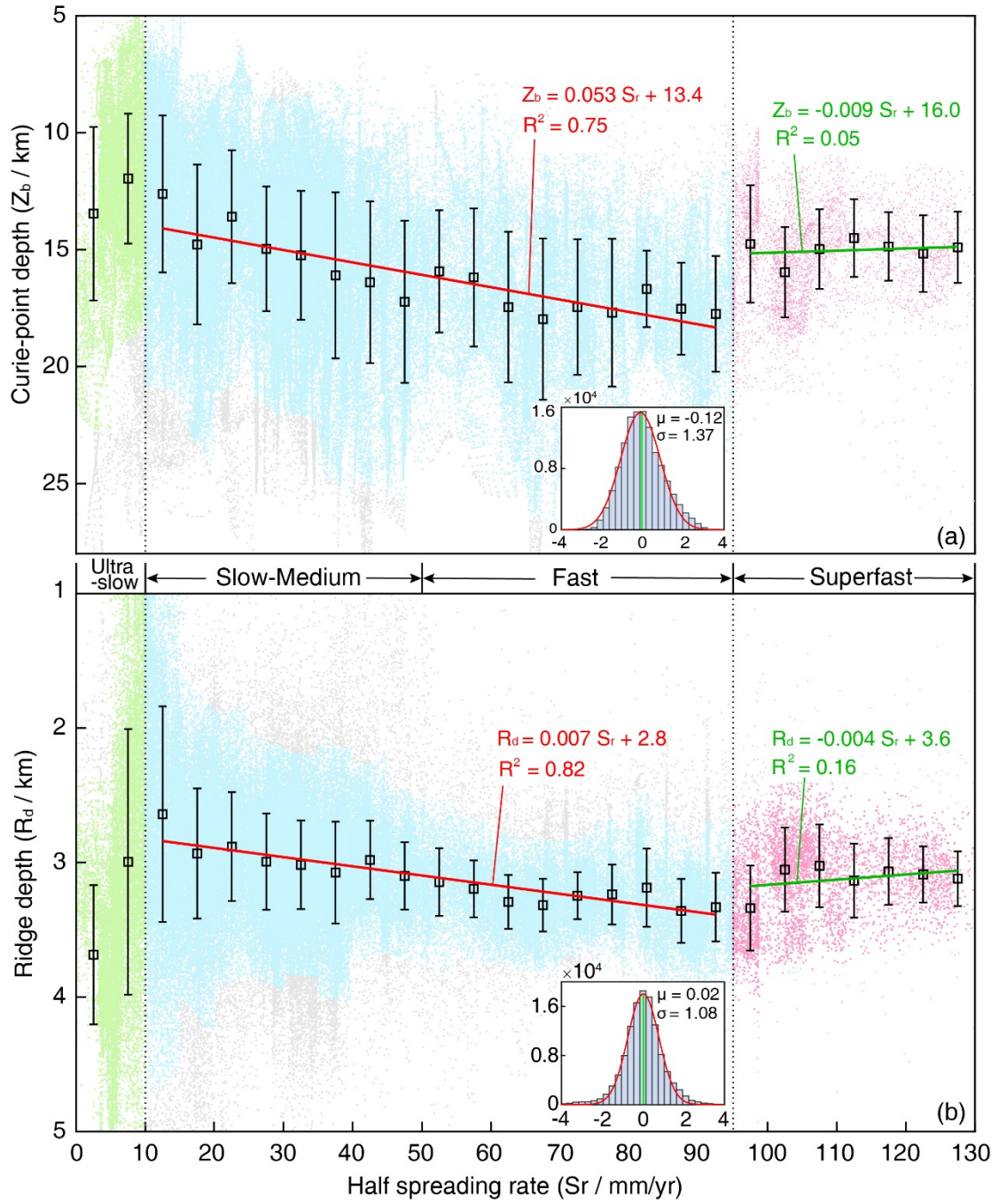


**Fig. 8** Curie point depth and ridge depth correlation with spreading rate. The red and green solid lines are linear regressions of mean values of  $Z_b$  and  $R_d$  for  $10 < S_r < 95$  mm/yr and  $S_r > 95$  mm/yr, respectively. Other label interpretations refer to Fig. 4



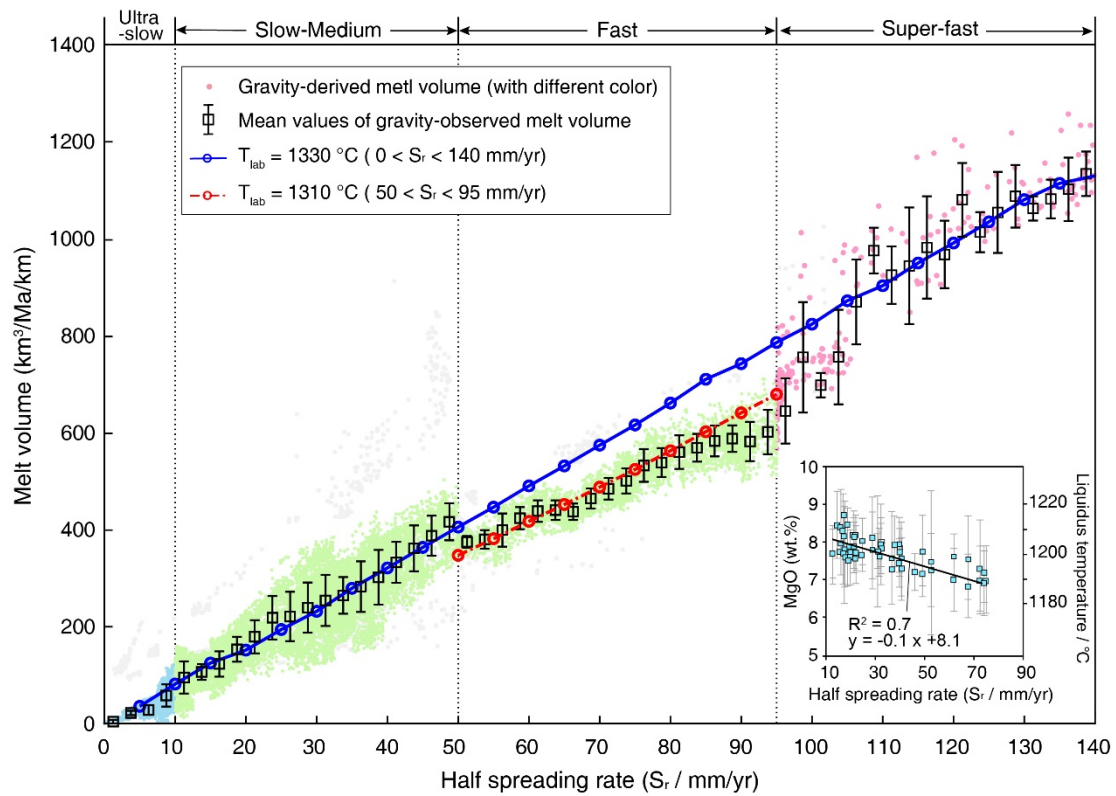


**Fig. 9** Melt volume variation with half spreading rate along mid-ocean ridges within 1 Ma isochrons for a 1 km length segment. Blue and red solid lines with corresponding circles are from numerical modeling at different spreading rates. Other label interpretations refer to Fig. 5

## APPENDIX B: Melt volume from gravity observation and numerical modeling

### B.1 Observed melt volume

Our observed melt volume at a mid-ocean ridge (MOR) is an upper bound on the volume of crust, as it assumes 100% melt extraction. A transect of MOR is defined to be 1 km long along the ridge and within 1 Ma isochrons. Thus, the unit of melt volume is  $\text{km}^3/\text{km}/\text{Ma}$ . The transect area =  $(S_r \times 1 \text{ Ma}) \times 1 \text{ km}$ , where  $S_r$  is the half spreading rate. Then melt volume is the product of crustal thickness and the area of transect.

### B.2 Numerical modeling of melt volume

Here melt volume is computed using a numerical model. The model is governed by the equations of conservation of momentum, mass and energy (e.g. McKenzie, 1984), namely,

$$\begin{cases} -2\Delta \cdot (\eta \nabla^s \mathbf{u}) + \nabla p = \rho \mathbf{g} & (1a) \\ \nabla \cdot \mathbf{u} = 0 & (1b) \\ \rho C_p \left( \frac{\partial T}{\partial t} + \mathbf{u} \cdot \nabla T \right) = \nabla \cdot (k \nabla T) + \rho f & (1c) \end{cases}$$

where  $\eta$  is the viscosity,  $\nabla^s$  the symmetrized gradient,  $\mathbf{u}$  the velocity,  $p$  the pressure,  $\rho$  the density,  $\mathbf{g}$  the gravity acceleration,  $C_p$  the heat capacity,  $T$  the temperature,  $k$  the thermal conductivity and  $f$  a heat source term. Bold symbols denote vectorial quantities.

666 Rheology is assumed to be viscous and is governed by two power laws for  
667 dislocation and diffusion creep deformation mechanisms, which are combined using a  
668 harmonic mean to produce an effective viscosity. Rheological parameters are taken  
669 from Hirth and Kohlstedt (2003). The heat capacity is set to be a constant ( $1000 \text{ J} \cdot \text{kg}^{-1} \cdot \text{K}^{-1}$ ),  
670 whereas thermal expansion coefficient and thermal conductivity are dependent  
671 on temperature and pressure (Fei, 1995 and Hofmeister 1999, respectively). The main  
672 phase transitions of olivine are included in the model (olivine, wadsleyite,  
673 ringwoodite and Mg-perovskite). The stability field of these mineral phases is  
674 parameterized based on their Clapeyron slopes and the density is modified  
675 accordingly (Guest et al. 2004; Katsura and Ito 1989; Katsura et al. 2004).

676 The heat source term,  $f$ , includes the following contributions,

$$f = f_s + f_a + f_t \quad (2)$$

677  $f_s = \sigma_{ij} \epsilon_{ij} \quad (3)$

$$f_a = T \alpha \rho u_z g \quad (4)$$

678 The term  $f_s$  accounts for the viscous dissipation, and  $\sigma_{ij}$  and  $\epsilon_{ij}$  are the stress and strain  
679 rate tensors respectively. The term  $f_a$  includes the heat changes due to adiabatic  
680 compression and decompression of materials.  $\alpha$  is the thermal expansivity,  $u_z$  is the  
681 vertical component of velocity, and  $g$  is the vertical component of gravity vector.  
682 Finally, the term  $f_t$  ( $10\text{E-}8 \text{ W} \cdot \text{m}^{-3}$ ) includes the radiogenic heating due to the decay of  
683 radioactive isotopes in the mantle composition.

684 The space discretization of equations (1a) and (1b) is done via mixed finite  
685 elements with unknowns of velocity and pressure (Donea and Huerta 2002). The

interpolation is quadratic for velocities and linear for pressure, therefore guaranteeing the numerical stability of the solution. Temperatures are computed from Eq. (1c) and are interpolated using linear elements. Time discretization is done using a two-stage Padé method of second order.

The space domain represents one half spreading center with a width and height of 660 km (Fig. 10). The computational mesh is composed by non-uniformly distributed triangles, with a maximum resolution at ridges, where element size is 2.5 km length. Then the size of triangles gets larger with increasing depth and distance to the ridges.

Surface temperatures are imposed to be 0 °C at the surface and 1607 °C at the bottom (660 km depth) based on a potential temperature of 1277°C and an adiabatic gradient of 0.5 °C km<sup>-1</sup>. Note that despite temperature fields in Fig. 11 are shown in the region of interest (until 100 km depth), the model goes down to 660 km depth. Heat flux is zero on the lateral walls. The initial temperature corresponds to a half-space cooling model (Afonso et al. 2008). The spreading rate is imposed as a boundary condition on the surface, while velocity is free-slip on the other three walls of the computational domain.

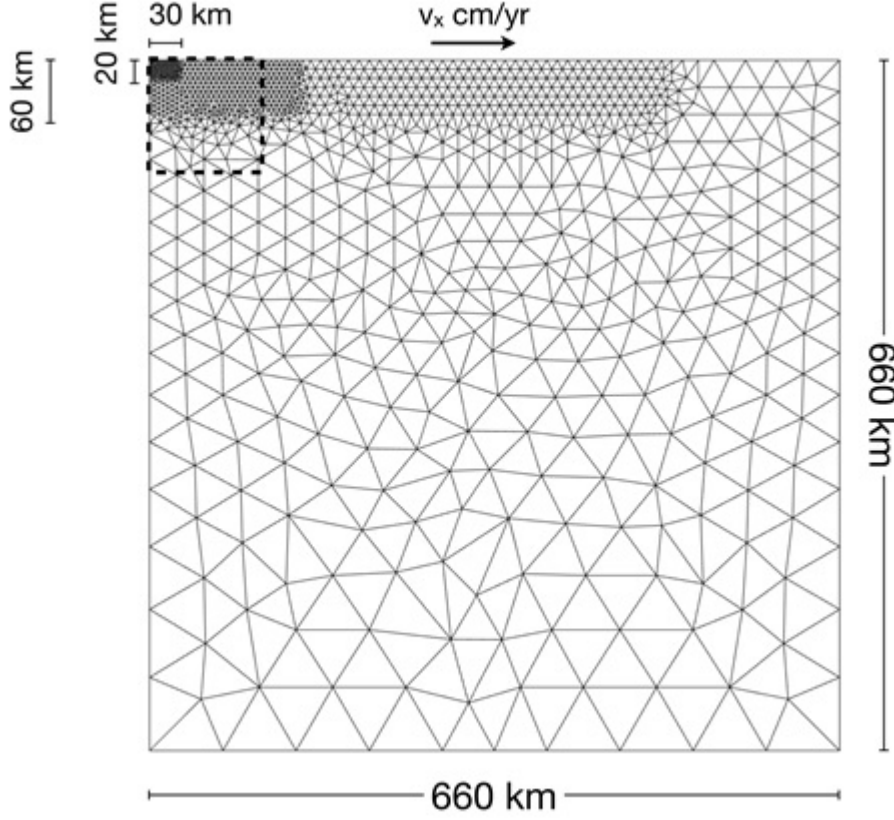


**Fig. 10** Computational domain of half mid ocean ridge (located at the left). The dashed line marks the area shown in Fig. 11

Melting is computed as a post process of temperatures and pressures using the model (and the code) of Katz et al. (2003). The melt fraction is defined as:

$$F(P, T, X_{H_2O}^{bulk}) = \begin{cases} \left[ \frac{T - (T_{solidus}(P) - \Delta T(X_{H_2O}(X_{H_2O}^{sat}, P, F)))}{T_{liquidus}^{lerhz}(P) - T_{solidus}(P)} \right] \gamma_1, (X_{H_2O} > X_{H_2O}^{sat}) \\ \left[ \frac{T - (T_{solidus}(P) - \Delta T(X_{H_2O}(X_{H_2O}^{bulk}, P, F)))}{T_{liquidus}^{lerhz}(P) - T_{solidus}(P)} \right] \gamma_1, (F < F_{cpx-out}) \\ F_{cpx-out} + (1 - F_{cpx-out}) \left[ \frac{T - T_{cpx-out}}{T_{liquidus} - T_{cpx-out}} \right] \gamma_2, (F > F_{cpx-out}) \end{cases} \quad (4)$$

710 where  $X_{H_2O}$  is the weight fraction of water dissolved in the melt,  $X_{H_2O}^{bulk}$  the total  
 711 weight fraction of water,  $T_{cpx-out}$  the temperature when cpx is totally dissolved,  $T_{solidus}$   
 712 the solidus temperature of mantle,  $T_{liquidus}$  the liquidus temperature of mantle,  $T_{liquidus}^{lherz}$   
 713 the liquidus temperature of lherzolite,  $\Delta T(X_{H_2O})$  the temperature variation due to the  
 714 bulk water,  $F_{cpx-out}$  the weight fraction of F when cpx is totally dissolved,  $\gamma_1$  and  $\gamma_2$   
 715 the exponents of melt function.

716 Finally, melt volume is obtained by integrating the melt fraction  $F$  in the region  
 717 within 1 Ma isochrons. This melt volume is assumed to be constant along the ridge  
 718 and thus, it corresponds to a ridge transect of 1 km long. The models run until a  
 719 steady state is obtained and melt fraction does not change with time. The final  
 720 temperature distributions do not depend on the initial temperature condition, which  
 721 just vary at different spreading centers. Snapshots of temperatures and melt fraction  
 722 are show in Fig. 11.

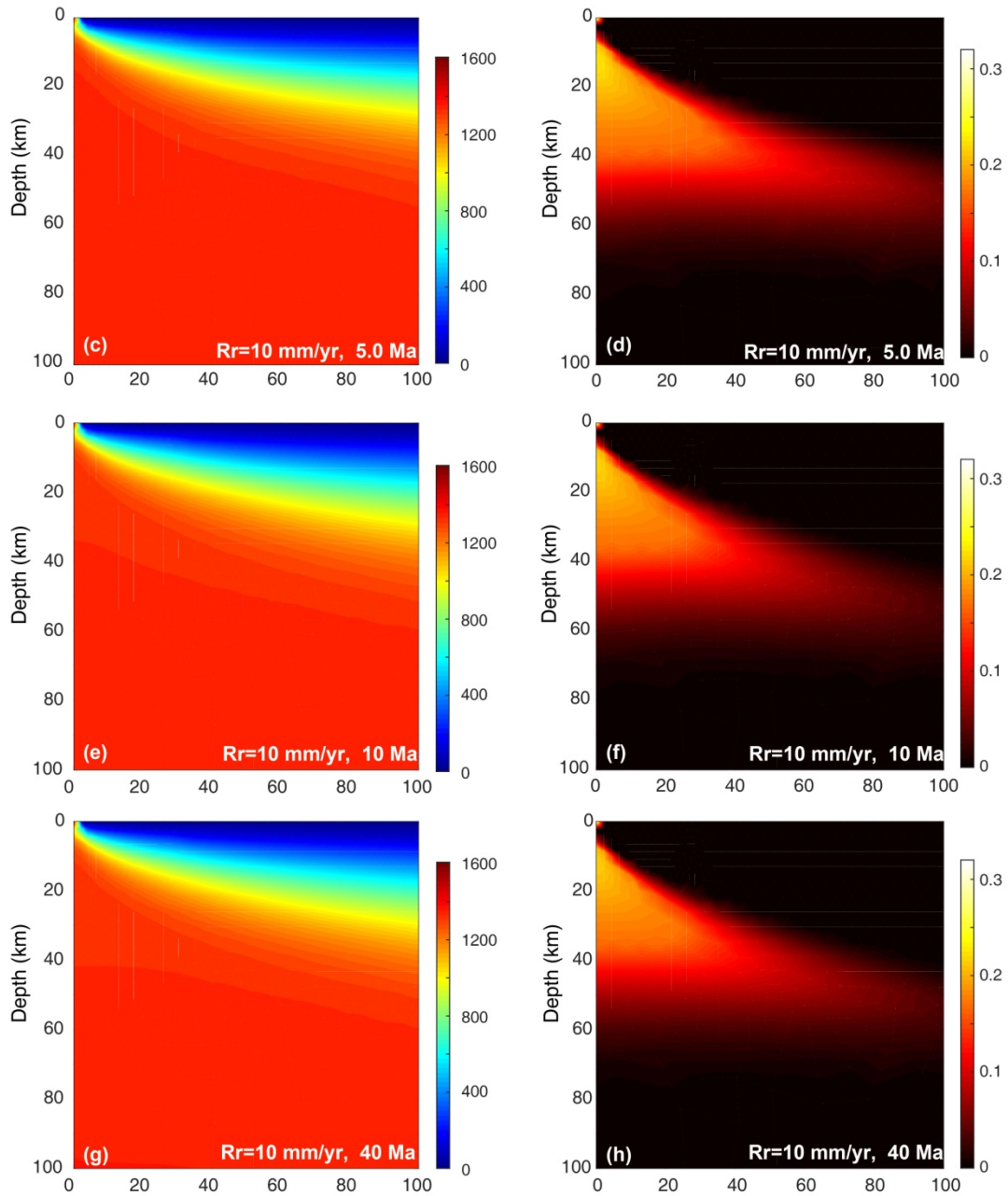


**Fig. 11** Snapshots of modelled temperature (a), (c), (e), (g) and melt fraction (b), (d), (f), (h) of a mid-ocean ridge at a spreading rate  $R_r = 10$  mm/yr. Area shown corresponds to the ridge region where partial melting occurs. Melting field becomes steady after 10 Ma of seafloor spreading

## References

- Afonso JC, Zlotnik S, Fernández M (2008) Effects of compositional and rheological stratifications on small-scale convection under the oceans: Implications for the thickness of oceanic lithosphere and seafloor flattening. *Geophys Res Lett* 35 doi:10.1029/2008gl035419
- Bown JW, White RS (1994) Variation with spreading rate of oceanic crustal thickness and geochemistry. *Earth Planet Sci Lett* 121:435-449
- Chen YJ (1992) Ocean crustal thickness versus spreading rate. *Geophys Res Lett* 19:753-756 doi:<https://doi.org/10.1029/92GL00161>
- Dick HJB, Erzinger JA, Stokking LB (1992) Proceedings of the ocean drilling program. Texas A&M University, College Station, Tex.
- Dick HJB, Lin J, Schouten H (2003) An ultraslow-spreading class of ocean ridge. *Nature* 426 405–412 doi:10.1038/nature02128
- Donea J, Huerta A (2002) Finite Element Methods for Flow Problems. Wiley, West Sussex PO19 8SQ, England
- Guest A, Schubert G, Gable CW (2004) Stresses along the metastable wedge of olivine in a subducting slab: possible explanation for the Tonga double seismic layer. *Phys Earth Planet Inter* 141:253-267 doi:10.1016/j.pepi.2003.11.012
- Hirth G, Kohlstedt D (2003) Rheology of the upper mantle and the mantle wedge: A view from the experimentalists, in *Inside the Subduction Factory*. In: Eiler J (ed) *Geophysical Monograph Series*, vol 138. American Geophysical Union, Washington, D. C., pp 83 – 105
- Hofmeister AM (1999) Mantle values of thermal conductivity and the geotherm from phonon lifetimes. *Science* 283 doi:<https://doi.org/10.1126/science.283.5408.1699>
- Katsura T, Ito E (1989) The system  $\text{Mg}_2\text{SiO}_4$  -  $\text{Fe}_2\text{SiO}_4$  at high pressures and temperatures\_ Precise determination of stabilities of olivine, modified spinel, and spinel.pdf>. *J Geophys Res* 94:15,663-615,670
- Katsura T et al. (2004) Olivine-wadsleyite transition in the system  $(\text{Mg,Fe})_2\text{SiO}_4$ . *J Geophys Res Solid Earth* 109 doi:10.1029/2003jb002438
- Katz RF, Spiegelman M, Langmuir CH (2003) A new parameterization of hydrous mantle melting. *Geochem Geophys Geosyst* 4:n/a-n/a doi:10.1029/2002gc000433
- Li C-F, Lu Y, Wang J (2017) A global reference model of Curie-point depths based on EMAG2. *Sci Rep* 7:45129 doi:10.1038/srep45129
- Reid I, Jackson HR (1981) Oceanic spreading rate and crustal thickness. *Mar Geophys Res* 5:165-172 doi:<https://doi.org/10.1007/BF00163477>
- Umino S, Crispini L, Tartarotti P, Teagle DAH, Alt JC, Miyashita S, Banerjee NR (2008) Origin of the sheeted dike complex at superfast spread East Pacific Rise revealed by deep ocean crust drilling at Ocean Drilling Program Hole 1256D. *Geochem Geophys Geosyst* 9:n/a-n/a doi:10.1029/2007gc001760
- White RS, McKenzie D, O'Nions RK (1992) Oceanic crustal thickness from seismic measurements and rare earth element inversions. *J Geophys Res* 97 doi:10.1029/92jb01749
- White RS, Minshull TA, Bickle MJ, Robinson CJ (2001) Melt generation at very slow-spreading oceanic ridges: constraints from geochemical and geophysical data. *J Petrol* 42:1171–1196 doi:<https://doi.org/10.1093/petrology/42.6.1171>